Hydrogen in Silicon Solar Cells: The Role of Diffusion

Jonas Schön, Phillip Hamer, Benjamin Hammann, Christoph Zechner, Wolfram Kwapil, and Martin C. Schubert*

A model for hydrogen in silicon is presented, which accounts for both in-diffusion and out-diffusion from a passivation layer (e.g., SiN$_x$), as well as the known hydrogen reactions within the silicon matrix. The model is used to simulate hydrogen diffusion and reactions during contact firing in a solar cell process, with a particular focus on variations in the cooling process, the sample thickness, and boron doping levels. The model reproduces the measured differences in hydrogen concentration due to these variations and thus helps to understand hydrogen-induced surface degradation and the dependencies of light and elevated temperature-induced degradation (LeTID) on the cooling process due to the close relation of LeTID and hydrogen. The same model and parameters are utilized to simulate the subsequent annealing of the fired samples at temperatures ranging from 160 to 290 °C. By successfully modeling the development of boron–hydrogen pairs during dark annealing processes across varying temperatures and doping levels, it is demonstrated that diffusion toward the Si/SiN$_x$ interface explains the observed decrease in resistivity and reductions in boron–hydrogen concentrations over extended dark annealing durations. Our simulations show the necessity of considering the depth-dependent hydrogen distributions after the firing process for analyzing the dark annealing.

1. Introduction

Over the past decades, the diffusion of hydrogen in thick silicon wafers and the dynamics of molecular hydrogen and boron–hydrogen (BH) pairs have been intensively studied.[1–8] Hydrogen passivation is a key technique in the fabrication of high-efficiency solar cells, capable of passivating both bulk defects and, most importantly, silicon interfaces. The clear correlation between hydrogen concentration and light and elevated temperature-induced degradation (LeTID)[9–11] has further enhanced the research efforts and ignited interest in controlling the hydrogen distribution. Although empirical solutions for reducing LeTID have been developed in recent years, such as slightly decelerating the cooling process after contact firing[12–14] or implementing rapid regeneration techniques,[15–17] the underlying physical mechanisms remain elusive.[18]

Following the discussions on LeTID, our understanding of hydrogen complex formation and diffusion in silicon has advanced. Voronkov et al.[19] and Hamer et al.[20] proposed models to elucidate hydrogen dynamics, incorporating H-charge states, hydrogen molecules (H$_2$), and BH pairs. However, more recent annealing experiments (e.g., [21]), following conventional contact firing processes, have demonstrated a significantly faster H$_2$ dissociation compared to [19]. Rodrigues et al.[22] updated these parameters using a comprehensive experimental dataset that includes variations in hydrogen and dopants, further enriched by additional literature data,[23,24] particularly concerning temperature variations.

Two aspects of hydrogen kinetics have been the subject of contentious debate in the literature: 1) the observed decrease in BH concentration (or increase in hole concentration) during prolonged annealing experiments in the dark, attributed to another H-molecule "H$_{2C}$" in ref. [19], and 2) the diffusivity of atomic hydrogen, which has shown considerable variance across experimental results.[8,25–27] While an additional fast-diffusing neutral atomic hydrogen species at the antibonding side, as predicted by ab initio calculations,[25] could account for the observed accelerated diffusivity of atomic hydrogen at moderate temperatures, no additional evidence has yet been found to support the existence of a H$_{2C}$ molecule. The reaction kinetics of the increase in hole concentration during extended annealing experiments was examined in ref. [22], revealing a linear dependence of the reaction rate on atomic hydrogen, which counters the theory of molecular formation.

Pritchard et al.[28] observed an increase in the concentration of vacancy-hydrogen complexes (VH$_4$) as BH pairs diminished. Additionally, we noted in ref. [18] that the BH-pair dissociation and the surge in surface-related charge carrier recombination

J. Schön, B. Hammann, W. Kwapil
INATECH, Chair for Photovoltaic Energy Conversion
University of Freiburg
Emmy-Noether-Str. 2, 79110 Freiburg, Germany
E-mail: jonas.schoen@inatech.uni-freiburg.de

J. Schön, B. Hammann, W. Kwapil, M. C. Schubert
Division Photovoltaics
Fraunhofer Institute for Solar Energy Systems ISE
Heidenhofstr. 2, 79110 Freiburg, Germany

P. Hamer
School of Photovoltaic and Renewable Energy Engineering
The University of New South Wales
Sydney, NSW 2052, Australia

C. Zechner
Synopsys GmbH
Karl-Hammerschmidt-Str. 34, Aschheim 85609, Germany

rates typically occur simultaneously, and the speed of this process is influenced by wafer thickness. These observations align with findings from refs. [29,30], where effusion experiments and SIMS measurements were combined. They concluded that, upon annealing, hydrogen atoms released from BH pairs in the bulk material do not exit the sample but rather accumulate in the sub-surface area, where they form Si—H bonds. First process models that combine hydrogen reactions and diffusion implemented in the scripting language of Synopsys process simulator Sentaurus Process[31] have already demonstrated promising outcomes.[32,33] In this article, we introduce a 2D hydrogen model based on these approaches and determine the model parameters using experimental data. The focus is on the universal applicability of the model and the attempt to describe all experimental findings with the smallest possible set of parameters.

2. Model

Building on the models proposed by Hamer et al. and Hammann et al. a 1D hydrogen model for boron-doped silicon was developed. This model facilitates both diffusion from and into a silicon nitride (SiN_x) layer stack. Within the silicon matrix, three charge states of hydrogen $H^{+/0/-}$ are considered. The neutral state, H^0, offers an effective representation of the states $H^{0,T}$ and $H^{0,AB}$ identified in ab initio calculations.[25] As demonstrated in ref. [33], we fit the diffusivity $D_{H^0, \text{eff}}$ of this effective H^0 state (see **Table 1**). This chapter outlines the model concerning charge carriers in equilibrium without illumination. For the illuminated scenario, the corresponding equations are summarized in the Supporting Information.

An equilibrium state between the three hydrogen charge states is assumed in all simulations and is calculated as follows

$$[H^0] = \frac{[H]}{1 + 0.5 \times \exp\left((0.5 \times E_g - 0.16eV)/(k_B T)\right) \times p/n_i + 0.25 \times \exp\left((0.5 \times E_g - 0.46eV)/(k_B T)\right) \times n/n_i} \quad (1)$$

Table 1. Model parameters for the H/H$_2$/BH system.

Material	Parameter	Used equation/quantity	Origin
Si	D_{H^+}	$4.24 \times 10^{-4} \text{cm}^2\text{s}^{-1} \exp\left(-\frac{0.43eV}{k_B T}\right)$	[42]
	$D_{H^0, \text{eff}}$	$2.2 \times 10^{-3} \text{cm}^2\text{s}^{-1} \exp\left(-\frac{0.11eV}{k_B T}\right)$	Fit
	D_{H^-}	$1.3 \times 10^{-2} \text{cm}^2\text{s}^{-1} \exp\left(-\frac{0.7eV}{k_B T}\right)$	[43]
	D_{H_2}	$2.6 \times 10^{-4} \text{cm}^2\text{s}^{-1} \exp\left(-\frac{0.78eV}{k_B T}\right)$	[20]
	α_{BH}	$2.5 \times 10^{15} \text{s}^{-1} \exp\left(-\frac{1.4eV}{k_B T}\right)$	Fit
	α_{H_2}	$1.7 \times 10^{-9} \text{cm}^3\text{s}^{-1} \exp\left(-\frac{1.1eV}{k_B T}\right)$	Fit
	$\beta_{H^+H^0}$	$2 \times 10^{-10} \text{cm}^3\text{s}^{-1} \exp\left(-\frac{0.45eV}{k_B T}\right)$	Fit
	$\beta_{H^+H^-}$	$8 \times 10^{-10} \text{cm}^3\text{s}^{-1} \exp\left(-\frac{0.2eV}{k_B T}\right)$	Fit
L_{Segre}/Si	$k^0_{H(L_{Segre}/Si)}$	$0.02 \exp\left(-\frac{0.9eV}{k_B T}\right)$	Fit
L_{Segre}	$Sol_{H(L_{Segre})}$	$2 \times 10^{35} \text{cm}^{-3} \exp\left(-\frac{3eV}{k_B T}\right)$	Fit

$$[H^+] = 0.5 \times \exp\left(\frac{0.5 \times E_g - 0.16eV}{k_B T}\right) \times p/n_i \times [H^0] \quad (2)$$

$$[H^-] = 0.25 \times \exp\left(\frac{0.5 \times E_g - 0.46eV}{k_B T}\right) \times n/n_i \times [H^0] \quad (3)$$

with the total atomic hydrogen concentration [H], the electron (hole) concentration n (p), the intrinsic density n_i, the Boltzmann constant k_B, temperature T, and the bandgap E_g. The prefactors for $H^{-/+}$ are taken from ref. [25]. The reaction between positive hydrogen H^+ and B^- is described in [22]

$$\frac{d[BH]}{dt} = \beta_{BH} \times [H^+][B^-] - \alpha_{BH} \times [BH] \quad (4)$$

with[34]

$$\beta_{BH} = \frac{e^2 D_{H^+}}{\varepsilon_{Si} k_B T} \quad (5)$$

and the silicon permittivity ε_{Si} and the electric charge e. The fitted reaction rate α_{BH} with an activation energy of 1.4 eV, which is 0.12 eV higher compared to the most common literature value,[20,35] and the diffusivity of positive hydrogen D_{H^+} are presented in Table 1. Based on the ab initio calculations of Gomes et al.[25] only one type of hydrogen molecule H_2 is implemented. This is in line with ref. [22], where a proportionality of the reaction rate to the atomic hydrogen concentration was found. The change in the H_2 concentration is described by the reactions

$$\frac{d[H_2]}{dt} = [H^+] \times (\beta_{H^+H^0}[H^0] + \beta_{H^+H^-}[H^-]) - \alpha_{H_2} \times p \times [H_2] + D_{H_2}\nabla\nabla[H_2] \quad (6)$$

The fitted activation energy of α_{H_2} (see Table 1) is between the values of 1.05 and 1.15 eV found in different analyses.[22,36] In contrast to previous models,[8,20,22,37] we included a reaction of H^+ and H^- in our model, which becomes negligible in p-type silicon for temperatures below 300 °C and is discussed in the Supporting Information. The used fit parameters $\beta_{H^+H^0}$ and $\beta_{H^+H^-}$ and the molecule diffusivity D_{H_2} are summarized in Table 1.

Figure 1 illustrates the dominant mechanisms in the proposed model for boron-doped silicon at various temperatures. During the peak temperature phase of the contact firing process, an in-diffusion of hydrogen from SiN_x is observed. At lower
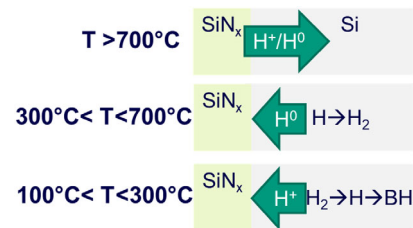

Figure 1. Schematic overview of the dominant hydrogen processes at the Si surface and bulk. Keep in mind that the temperatures only give rough ranges and that the dominant reactions in silicon depend strongly on the doping.

temperatures, hydrogen diffuses out of the Si wafer. Slowing the cooling process results in substantially lower hydrogen concentrations within the silicon wafer.[18]

In our model, we characterize the phenomenon at the SiN_x/Si interface using a segregation equation that describes the exchange between atomic hydrogen in silicon (H_{Si}^0) and a segregation layer L_{Segre} ($H_{L_{segre}}$)

$$\frac{dH_{Si}}{dt} = -\frac{dH_{L_{segre}}}{dt} = t_{H\left(L_{segre}/Si\right)} \times \left(H_{L_{segre}} - \frac{H_{Si}^0}{k_{H\left(L_{segre}/Si\right)}^0} \right) \quad (7)$$

using a temperature-dependent segregation coefficient $k_{H\left(L_{segre}/Si\right)}^0$, which is independent of the charge carrier density on the silicon side (see Table 1). The transfer coefficient $t_{H\left(L_{segre}/Si\right)}$ is chosen so as not to limit the process. The atomic hydrogen concentration in the segregation layer $H_{L_{segre}}$ is constrained by its solubility in the segregation layer, denoted as $Sol_{H\left(L_{segre}\right)}$.

In the model presented in this paper, the segregation of hydrogen into the segregation layer and the associated depletion of hydrogen at the silicon surface is the driver for hydrogen diffusion from silicon bulk toward the surface. In the cases simulated in Section 3, the segregation layer serves most of the time as either an almost infinite source or sink for hydrogen, depending on the process temperature. Thus, the process is limited by the diffusion of hydrogen in the silicon bulk.

Since there are no direct hydrogen measurements at the SiN_x/Si interface available, it is not possible for us to distinguish whether hydrogen segregates into the surface passivation layer stack (here SiN_x) or agglomerates at the interface or in the vicinity of the interface.[22,29,30] This is the reason for our use of the term "segregation layer," in order to stress its functionality within our model framework rather than pinpointing the exact location of the hydrogen sink.

The initial hydrogen concentration in the segregation layer, i.e., the hydrogen concentration after deposition, depends strongly on the specific SiN_x composition and processing of the SiN_x. Other model parameters describing hydrogen in the SiN_x, i.e., temperature-dependent H diffusivity, H bonding to Ni and Si atoms (solubility of mobile hydrogen),[38] out-diffusion from SiN_x to the ambient, and the segregation coefficient, are not well known and are also expected to vary from SiN_x to SiN_x. With the given experimental data, no unambiguous parameter set for hydrogen in the segregation layer can be found. Furthermore, in the inhouse experiments,[18,22,33] an additional 5–10 nm AlO_x layer was deposited between SiN_x and silicon, where the AlO_x acts as a hydrogen sink, thereby reducing the effective hydrogen concentration in the layer. A comprehensive physical description of all mechanisms within the SiN_x and AlO_x layers requires additional experimentation and is beyond the scope of this paper.

As mentioned previously, we focus on the role of the effective segregation layer as a sink or source for hydrogen, simplifying the model: All sample-specific characteristics are summarized in the effective "initial H concentration" in the segregation layer, which is calibrated for each experimental set; other effects like out-diffusion into the ambient are neglected. The effective

Table 2. Initial hydrogen concentrations used in the model for the segregation layer.

Experiment	Reference	Initial [H] in the segregation layer
Firing with T-plateau	Figure 2[33]	4.9×10^{20} cm^{-3} (AlO_x/SiN_x)
Cooling ramp variation	Figure 3 and 4A[18]	6.8×10^{20} cm^{-3} (AlO_x/SiN_x)
T-peak variation "Winter et al."	Figure 4B[24]	1×10^{21} cm^{-3} (SiN_x)
T-dependent anneal "Acker et al."	Figure 5A[23]	2.7×10^{20} cm^{-3} (SiN_x)
T-dependent anneal "Winter et al."	Figure 5B[24]	2.3×10^{21} cm^{-3} (w/o intentional layer)
Doping variation	Figure 6 and 7[22]	$3.8–7.6 \times 10^{20}$ cm^{-3} (AlO_x/SiN_x)

hydrogen concentrations in the segregation layers used for modeling the various experiments (see **Table 2**) are smaller than the concentrations found in experimental studies for pure SiN_x.[38] Keep in mind that the effective hydrogen concentration in the segregation layer, as listed in Table 2, is the only parameter being fitted separately for the different experiments.

This paper focuses on 1D simulations and the diffusion of hydrogen from or toward the silicon surface. However, the model can also be utilized for the simulation of lateral H diffusion in a 2D or 3D structure. The agglomeration of hydrogen at point contacts, which causes an increase in the contact resistance, is shown in Section II, Supporting Information as an example.

3. Results

Various experiments are simulated across a broad temperature range and sample variations to fine tune critical parameters and ensure that dominant mechanisms are incorporated into the model. The fitting of firing processes, along with variations in the cooling rate, is employed to determine the segregation coefficient $k_{H\left(L_{segre}/Si\right)}^0$ at the Si/L_{segre} interface and the effective H^0 diffusivity $D_{H^0, eff}$ (Section 3.1). Additionally, the increase in resistivity during dark anneal, indicative of BH formation, is used to ascertain the temperature-dependent dissolution rate of H-molecules, α_{H_2}.

In a previous model presented in ref. [22], based solely on hydrogen reactions, the apparent disappearance of BH pairs, i.e., the decrease in resistivity, for long dark anneal durations had been explained by a hypothetical reaction of atomic hydrogen with an unknown component Y, forming a YH complex. The latter is reminiscent of the hydrogen dimer H_{2C} as proposed by Voronkov et al. to explain the BH pair disappearance.[19] Neither YH nor H_{2C} have been experimentally observed so far. In the following, we show that the disappearance of BH can be explained in a simple way by hydrogen diffusion toward the Si/L_{segre} interface.

The activation energy of the segregation coefficient $k_{H\left(L_{segre}/Si\right)}^0$ is determined from the experimental data from variations of the contact firing processes (Section 3.1). The splitting rate of BH

pairs α_{BH} and thus the temperature-dependent equilibrium ratio of H^+/BH, along with the H^+-dominated effective hydrogen diffusivity at low temperatures, are calibrated based on the resistivity decrease observed during extended dark anneals (Section 3.2). Experiments involving doping variations, discussed in Section 3.3, enable the determination of $\beta_{H^+H^0}$ and $\beta_{H^+H^-}$ at high temperatures. Starting with a literature value, α_{H_2} is fine tuned to match the measured H_2 fractions. The fitting is performed iteratively due to the dependencies of the parameters. Note that parameters that have been described in previous publications (α_{BH}, $\beta_{H^+H^0}$, D_H, . . .) are not changed or only slightly adjusted. Annealing experiments under illumination are utilized to assess $\beta_{H^+H^-}$ at lower temperatures (see Supporting Information).

In addition to the parameters that are kept constant throughout the paper, only the effective hydrogen concentration in the segregation layer, as listed in Table 2, needs to be adjusted to bring the simulations in line with the experimental data.

3.1. Variation of the Contact Firing Process

In the first step, we compare our model with the measurement results of samples after firing process variations, as published in [33]. In the experiment, boron-doped (1 Ω cm) 252 μm-thick Fz samples underwent three distinctly different firing processes with a peak temperature at 800 °C (see inset in **Figure 2**B): 1) with a very rapid cooling ramp, 2) with an additional 5.5 s temperature plateau at 560 °C, and 3) with an additional 5.5 s temperature plateau at 660 °C. Subsequently, the BH and H_2 concentrations of some samples were measured with fourier-transform infrared spectroscopy (FT-IR), while other samples were annealed at 175 °C in the dark to determine changes in BH concentration via conductivity over time (see Figure 2B). The increase in resistivity at the 175 °C anneal is explained by the dissolution of H_2 molecules (Equation 6) and the subsequent BH pairing (Equation 4). Consequently, the maximum change in the BH concentration should be twice the originally measured H_2 concentration. For some samples, however, this BH change exceeds

expectations, and thus, we typically report both quantities when comparing total hydrogen concentrations. Additional sample and measurement details are available in ref. [33].

The hydrogen concentrations measured in these experiments were utilized to calibrate the activation energy for the diffusivity of H^0 in analogy to ref. [33]. The hydrogen diffusion toward the Si surface during the sample cooling is dominated by the H^0 diffusion as shown in [33], and thus, the effective H^0 diffusivity can be fitted. The determined activation energy was slightly lower than in [33] due to differences in α_{BH} that also influence the effective diffusivity of hydrogen. In Figure 2, we used our model to simulate the dependency of the total hydrogen concentration from the temperature of the 5.5 s plateau. At temperatures above 720 °C, the model forecast further in-diffusion of hydrogen from the segregation layer, resulting in a higher depth-averaged hydrogen concentration compared to the firing profile without a plateau. At lower temperatures, the segregation layer become a hydrogen sink, leading to a decrease in final hydrogen concentration in silicon due to out-diffusion during the plateau period. The hydrogen out-diffusion process is diffusion limited, causing the final hydrogen concentration to increase again at lower temperatures until a 5.5 s plateau had minimal impact, and a final hydrogen concentration similar to the rapid-firing process was attained.

In addition to modeling the total hydrogen concentration directly after the firing process, subsequent dark annealing was also simulated (see Figure 2B). The hydrogen distribution in our simulations of the dark annealing process was dominated by two mechanisms: 1) the dissolution of hydrogen molecules, controlled by the parameter α_{H_2}, and 2) the out-diffusion of atomic hydrogen. The effective hydrogen diffusivity in this temperature range is dominated by the diffusivity of positively charged hydrogen D_{H^+} and the fraction of atomic hydrogen, determined by the ratio α_{BH}/β_{BH} and the doping concentration.

A reasonable agreement between measurements and simulations was achieved for both the total concentration after the three different firing processes and BH concentrations during subsequent dark annealing. The BH concentration after the firing
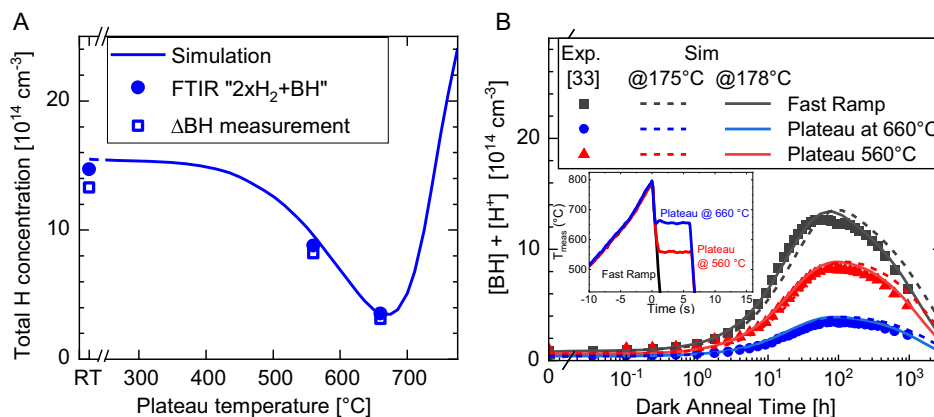

Figure 2. A) Simulated depth-averaged H concentrations after contact firing at max. 800 °C and cool down with 5.5 s plateau at varying temperatures. The total concentrations calculated from the BH and H_2 FT-IR signals in ref. [33] and the measured ΔBH after subsequent dark annealing for the two experiments with plateau and the firing process without plateau, i.e., plateau at room temperature (RT), are shown for comparison. B) Simulated (lines) and measured (symbols) reduction of the effective doping by BH pairing and H^+ during dark anneal subsequent to a firing process with a 5.5 s temperature plateau at 660 °C, 560 °C, or without temperature plateau.

process could not be directly measured at the wafer subjected to dark annealing; hence, we used the simulated BH concentration after the firing process as the initial BH concentration for the dark anneal experiment depicted in Figure 2B.

An initial hydrogen concentration of 4.9×10^{20} cm^{-3} in the segregation layer was fitted. All other model parameters remain unchanged for the experimental data in this paper. However, we expect slight temperature variations across different dark anneal setups, even though the temperature remains stable within a single experiment. Consequently, we permitted minor temperature adjustments during the fitting process. The best agreement for the measured BH concentrations in Figure 2B was found when simulating a dark anneal at 178 °C (solid lines), slightly higher than the 175 °C stated in ref. [33] (dashed lines).

It should be noted that the cooling ramp and the resulting hydrogen depth profile after the firing process significantly impact the out-diffusion process during dark anneal. This effect is demonstrated by modeling the experiments from ref. [18], where two different firing processes were applied to boron-doped (1 Ωcm) samples of varying thicknesses (thick: ≈254 μm, thin: 152 μm): one process with a cooling ramp of ≈300 K s^{-1} and another with ≈30 K s^{-1} (see inset in **Figure 3**B for the firing profiles). The simulated depth profiles after the firing process varied significantly for the two thicker samples: A pronounced hydrogen depletion toward the surface was observed in the slowly cooled sample (solid blue line in Figure 3A), while the in-diffusion profile remained visible in the fast-cooled sample (solid red line). The hydrogen concentration at the wafer center was almost the same in both samples, although the depth-averaged concentration—i.e., the measurable concentration—was 2.4 times higher in the fast-cooled sample. Consequently, the out-diffusion during dark anneal after a fast-cooling process was more pronounced, with 27% of the hydrogen diffusing out during the first 278 h of dark anneal compared to only 7% after slow cooling (dashed lines in Figure 3A). As a result, a significant difference was expected between the total hydrogen concentration and the peak BH concentration during subsequent dark anneal for the fast-cooled sample, with this BH peak being reached

earlier compared to the slowly cooled sample. The model accurately replicated the progression and the extent of the measured effective doping during dark anneal of the two thick samples (see Figure 3B). Moreover, the much smaller changes in BH concentration in the thin (152 μm) sample were well predicted by the model. Keep in mind that the initial hydrogen concentration in the segregation layer is the same for all thicknesses (see Table 2) and the difference between the thick and the thin slowly cooled samples originates from the out-diffusion during both the firing and the dark anneal processes.

Besides the three p-type wafers, 200 μm-thick n-type Fz wafers were processed in ref. [18]. As expected, the depth-averaged total hydrogen concentration after the slow cooling process lay between that of the thin and the thick sample (symbols to the left in **Figure 4**A). However, the total hydrogen concentration in the fast-cooled 200 μm-thick n-type sample was by far the highest among all FT-IR measurements in this experiment. In ref. [18], the higher total hydrogen concentration in the n-type samples compared to the thick p-type sample was attributed to the different doping types. In contrast, the simulations (lines in Figure 4A) indicate that the doping had only a minor influence on the total hydrogen concentration after the firing process, because the dominant diffusion processes happen during high temperatures under (almost) intrinsic conditions. Instead, this result is an effect of the intricate interplay between wafer thickness and cooling rate. As can be seen in Figure 4A, at slow cooling rates, there is enough time for hydrogen out-diffusion if the wafer is thin enough. The dependence on thickness reverses for fast-cooled samples, where the hydrogen concentrations are higher toward the surface due to the short time for in-diffusion at high temperatures (compared to the red solid line in Figure 3A). Hence, on average, the H concentration is lower in thicker wafers compared to thin wafers. The simulations, considering typical wafer thicknesses as shown in Figure 4A, demonstrate that the hydrogen concentration is highly dependent on the cooling rate until rates reach 50 K s^{-1} or 150 K s^{-1} for wafer thicknesses of 254 μm or 120 μm, respectively. For slower-cooled samples, a slight increase in the cooling rate (<20%) can more

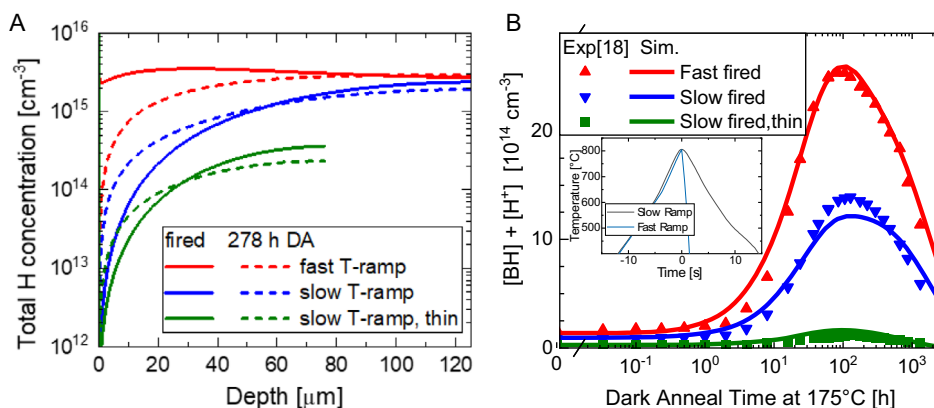**Figure 3.** A) Simulated hydrogen depth profiles after contact firing at max. 804 °C with a fast (≈300 K s^{-1}) and slow cooling (≈30 K s^{-1}) process (solid lines). The Si/L$_{Segre}$ interfaces of the 254 μm and 258 μm thick wafers are at a depth of 0 μm. The dashed lines show the simulated hydrogen profiles after subsequent dark annealing at 175 °C for 300 h. B) Sum of the simulated depth-averaged BH and H$^+$ concentrations during dark anneal subsequent to the two firing processes shown in the inset in comparison with the corresponding concentrations extracted from resistivity measurements (symbols, from refs. [18,22]).
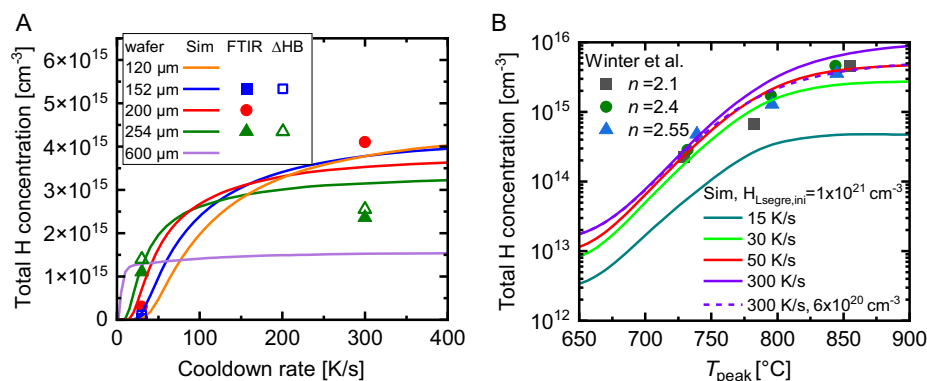
Figure 4. A) Depth-averaged simulated H concentration in silicon after contact firing process at max. 800 °C and cool down with varying cooling rates and wafer thicknesses. The total hydrogen concentrations calculated from the BH and H_2 FT-IR signals and the measured ΔBH after subsequent dark annealing from ref. [18] are shown for comparison. For simplicity, we show only simulations for a wafer thickness of 254 µm (green line), which was measured for the slowly cooled samples, although a thickness of 258 µm was measured for the thick fast-cooled sample. In the simulation, the total hydrogen concentration is only slightly affected by the doping type. Nevertheless, the n-type doping was considered in the simulation of the 200 µm thick wafer. B) Hydrogen concentration extracted from data presented by Winter et al.[24] measured after the firing process for different fire temperatures and SiN_x layers with different refractive indices n. The simulations show a similar trend but depend on the selected cooling rate and the initial hydrogen concentration in the segregation layer.

than double the hydrogen concentration, reflecting the strong cooling rate dependence of hydrogen-related LeTID defects.[12–14] Within the uncertainties, the measured hydrogen concentrations align well with the simulations.

Figure 4B illustrates the simulated hydrogen concentration postfiring as a function of peak firing temperature. For comparison, re-evaluated hydrogen concentrations from the experiment by Winter et al.[24] are included. Given that the precise temperature profiles of the wafers are unknown, a variation in cooling rates was executed. The experimentally observed strong dependence on peak temperatures between 650 and 850 °C was accurately mirrored by the model. The variations in the initial hydrogen concentration in the segregation layer for the fastest cooling rate (solid and dashed violet lines) demonstrate that the temperatures above which H in silicon saturates depend on the initial hydrogen concentration in the segregation layer and the cooling rate. The simulation demonstrates a strong dependence of the total hydrogen concentration with the peak temperature, showing an exponential-like relation in the important temperature region between 700 and 800 °C. Note that the LeTID extent, being closely connected to the H concentration, shows a similar exponential dependence on the peak firing temperature.[9]

To conclude Section 3.1, our model successfully explains the impact of a wide variety of firing profiles on the hydrogen distribution in silicon. The key feature is the change of the hydrogen flow direction at elevated temperatures (Figure 1), i.e., H diffusion toward the silicon surface during cool down, which we model with a temperature-dependent segregation coefficient between silicon and the segregation layer.

3.2. Variation of the Dark Annealing Temperatures

Next, we calibrate and test our model using resistivity measurements during dark annealing at various temperatures. The goal is

to demonstrate that the measured decrease of the resistivity during dark anneal can be reproduced with the modeled diffusion of H^+ toward the silicon surface only with slight adjustments of the literature value for α_{BH}, i.e., the ratio of H^+ and BH.

In **Figure 5**A, we simulate the processes published by Acker et al. in [23], in which 250 µm thick boron-doped (1 Ω cm) wafers underwent a firing process peaking at 750 °C. We assumed a typical cooling rate of 80 K s^{-1} until 550 °C, followed by a slower cool down to room temperature. Subsequently, the samples were annealed at temperatures ranging from 160 to 220 °C. The initial [H] in the segregation layer used for the simulations is provided in Table 2. The overall kinetics, with an increase in BH concentration in the beginning and a decrease at longer annealing durations, are well described by the simulation and thus in line with hypothesis that the latter is due to hydrogen out-diffusion. In particular, the model reproduces the measured BH concentrations during the 200 °C dark anneal, whereas the simulated BH changes at 220 °C are slower than the measurements. At first glance, this might be an indication of a higher activation energy in α_{H_2} and α_{BH}. However, it is crucial to consider that the results are highly sensitive to variations in wafer thickness and temperature: a mere 7 °C increase in dark anneal temperature could account for the discrepancies between the simulations and measurements, as illustrated by the blue dashed line in Figure 5A. For the 160 °C dark anneal, the simulation aligns well with the general trend and the BH concentration after firing. However, it underestimates the measured increase in BH, which could be due to sample-to-sample processing variations. Adjusting the peak firing temperature by an additional 9 °C resulted in a better match. The impact of these slight adjustments, both within the process uncertainty margins, gives an idea about the sensitivity of our model to the input parameters.

The simulations for the experiments by Winter et al.[24] carry even greater uncertainties. The samples were fired at 530 °C without a SiN_x layer prior to undergoing dark anneal at various temperatures. Consequently, the source of the hydrogen within
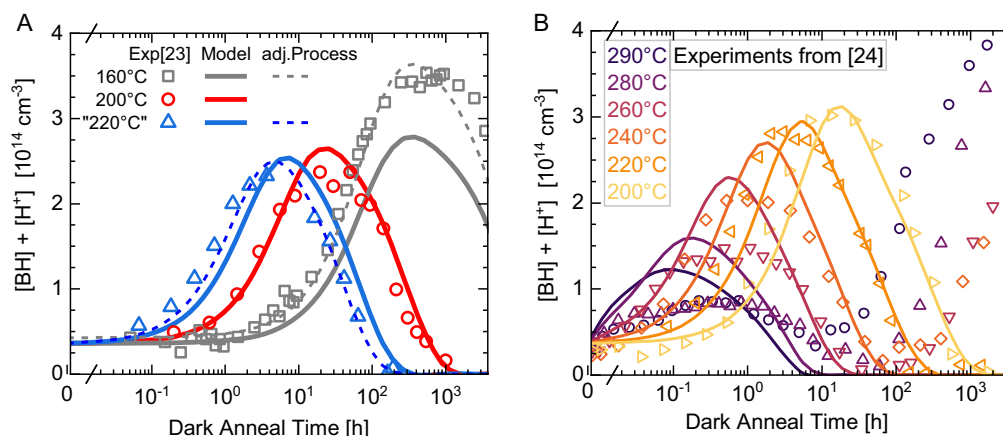
Figure 5. Simulated (solid lines) and measured reduction of effective doping by BH and H$^+$ during dark anneal at different temperatures. The concentrations are averaged over the wafer depth. A) Dark annealing of 250 µm-thick boron-doped wafers (see ref. [23] for details) after a firing process with 750 ± 10 °C peak temperature. The initial BH + H$^+$ concentrations were not measured in[23] and chosen to reach zero for very long annealing times. The dashed gray line shows a simulation with 759 °C peak temperature and the dashed blue line shows a simulation for dark anneal at 227 °C. B) Dark annealing at different temperatures of 250 µm-thick boron-doped wafers after annealing at 530 °C without SiN$_x$ coating (see ref. [24] for details).

the wafer post-530 °C anneal remains ambiguous and could differ across samples.[24] It is reported that hydrogen could be incorporated in the surface near region by wet chemical etching and cleaning steps.[39,40] Thus, we assume an in-diffusion from a thin (<1 µm) surface region during a firing process with 530 °C peak temperature and a cooling rate of 80 K s^{-1} for all samples in Figure 5B.

The model reliably captures the overall trends, such as the reduction in maximum BH concentration with increasing temperature. Most importantly, the kinetics of the decrease in BH concentration depending on temperature, which can be seen as a measure of the effective diffusivity of hydrogen, is well reproduced. Our interpretation of this result is, firstly, that the literature values of the H$^+$ diffusivity, which dominates in this case, give a good description even at these relatively low temperatures. Secondly, and more importantly, the temperature-dependent equilibrium ratio of H$^+$/BH seems to be well met by our model.

Clear discrepancies are observed between the measurements and simulations at higher dark anneal temperatures: At 280 °C and 290 °C, the maximum [BH] is reached much earlier in the simulations. Moreover, for these temperatures, along with 260 °C, the maximum BH concentration is overestimated. The deviations from Arrhenius behavior for H$_2$ dissolution in samples subjected to high annealing temperatures align with analyses in [22,24]. Moreover, these samples exhibit a significant resistivity increase after prolonged dark annealing, which is likely unrelated to BH. This resistivity increase commences earlier as the dark annealing temperature rises, artificially elevating the "[BH]+[H$^+$]" measurement below 10 h for the 280 °C and 290 °C samples, potentially explaining the discrepancies in hydrogen out-diffusion observed between measurements and simulations.

3.3. Variation of the Boron Concentration

So far, only boron-doped wafers with a resistivity of ≈1 Ω cm have been investigated. In this section, we simulate the

experiments from ref. [22] with doping variations between 2×10^{14} cm^{-3} and 7.2×10^{16} cm^{-3} to calibrate the doping dependence of the model. The ≈240 µm thick wafers, with a 5 nm AlO$_x$/150 nm SiN$_x$ layer stack, underwent a firing process reaching a maximum temperature of 800 °C with a cooling ramp of 80 K s^{-1}. The temperature profile of the firing process was measured for the sample with a boron concentration of 1.5×10^{16} cm^{-3}. To closely match the total hydrogen concentration after firing, we adjusted the effective hydrogen concentration in the segregation layer for each wafer separately (see Table 2) while maintaining the same temperature profile for all samples. However, we anticipate that the temperature profile might vary across samples due to differences in surface morphology or temperature fluctuations within the furnace. This temperature uncertainty significantly impacts the hydrogen concentration (see Figure 4) and may explain the observed differences between samples. According to FT-IR measurements,[22] the doping concentration itself has only a minor influence on the overall hydrogen concentration after the firing process. Given the uncertainty of the total hydrogen concentration, our focus is on reproducing the BH fraction, which is highly dependent on boron doping, and the resistivity development during dark anneal at 163 °C, i.e., [BH]+[H$^+$].

In **Figure 6**, both measured and simulated H$_2$ and BH concentrations after the firing process are presented for various boron concentrations. Above 600 °C, atomic hydrogen states predominate. Between 300 and 600 °C, H$_2$ forms from atomic hydrogen, while below 300 °C BH formation in boron-doped silicon forces the dissolution of molecules (see Figure 1 and, e.g., refs. [8,25,33]). Our model incorporates two reactions for H$_2$ formation (Equation 6): 1) by H$^+$ and H^0 as used in previous models[8,20,22,37] and 2) H$^+$ and H$^-$, which dominates for intrinsic conditions $n \approx p$, i.e., for low p-doped or n-doped samples, for high temperatures (>500 °C) and under illumination (see Supporting Information). The parameters for $\beta_{H^+H^0}$ and $\beta_{H^+H^-}$ (Table 1) are chosen to achieve reasonable agreement
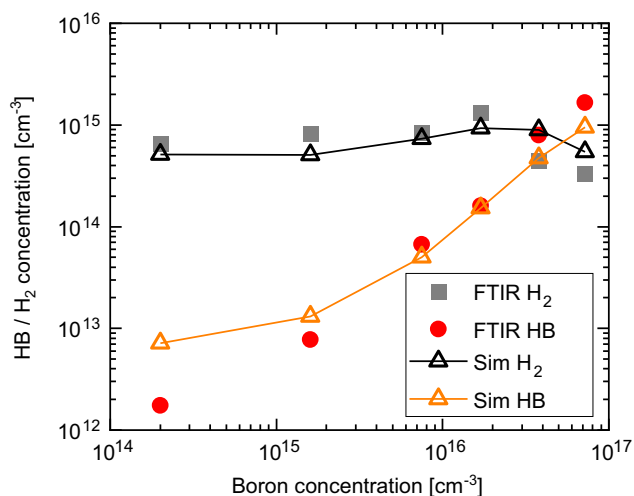
Figure 6. Simulated (open symbols) and measured (filled symbols) H_2 and BH concentrations in Fz wafers with varying doping concentrations after contact firing process with 800 °C peak temperature (experimental data from [22]).

of simulations and FT-IR measurements for the doping variation in Figure 6 and the other experiments in Section 3. The model predicts an almost linear dependency of BH from B for samples with a boron concentration much larger than the hydrogen concentration and thus reproduces the general trends observed in experiments. For lower boron doping, the model predicts a saturation as the fraction of hydrogenated boron atoms, i.e., [BH]/[B], increases.

At a closer look, the slope of the experimental data in Figure 6 is steeper compared to the simulations, and deviations are observed for the two highest-doped and the lowest-doped samples. Unfortunately, these three samples exhibit the highest measurement uncertainty. A possible explanation for this discrepancy is that the samples change over time even during dark storage at room temperature. The time between the firing process and FT-IR measurements was several months, whereas the dark annealing experiments were conducted shortly after the fast-firing step. Hence, the storage prior to the FT-IR measurements could have provided enough time for BH formation in the highly p-doped samples, especially if the samples were not stored entirely in the dark. This could also explain the discrepancies between FT-IR measurements and resistivity measurements

during dark anneal, which were already significant in this experiment: For samples with boron concentrations of 3.8×10^{16} cm^{-3} (7.2×10^{16} cm^{-3}), the change in resistivity during dark anneal indicate a BH increase of 1.8×10^{15} cm^{-3} (1.1×10^{15} cm^{-3}) which is a factor of 2 (1.7) higher than the hydrogen in H_2 measured by FT-IR. Due to these uncertainties and the sample-to-sample variations, no reliable initial BH concentrations for the measurements in the dark annealing experiment can be given. Thus, we set the initial BH concentrations in the experimental data in **Figure 7** to the simulated BH concentrations after the firing process to facilitate easy comparison of measurements and simulations during dark annealing.

The fastest increase in BH concentration during dark annealing is observed in the most heavily doped sample. For this sample, the BH concentration remains nearly constant for over 1000 h in both the experiment and the simulation. We expect significant out-diffusion of atomic hydrogen after 1500 h of dark annealing according to the model. Lower-doped samples are expected to exhibit earlier out-diffusion due to their higher [H]/[BH] ratio and consequently greater effective diffusivity. For the four medium and highly doped samples, the simulated formation of BH, its reduction due to diffusion to the silicon surface, and the maximum BH concentration align well with the measurements. Again, our model is able to explain the results of an entirely different variation with the same parameter set.

However, the model overestimates the maximum [BH] in the sample with low doping concentrations of 1.6×10^{15} cm^{-3}. Note that here, the resistivity changes are at least an order of magnitude smaller compared to the more heavily doped samples and the shape of the measured curves significantly differs from that of the latter. Clearly, the model does not fully account for the reactions that lead to changes in resistivity. We believe that the reactions responsible for the different curve shapes in the lower-doped samples are also present in the higher-doped ones but are overshadowed by the more pronounced BH increase, as previously discussed in [22]. A possible candidate for this reaction is the H_2B complex predicted by ab initio calculations in ref. [41] that can be formed by the caption of an H atom by a BH pair. Since in the lower-doped samples, the ratio [BH]/[B] increases significantly, a non-negligible BH concentration compared to the overall boron concentration would significantly enhance this H_2B formation and further affect the resistivity dynamics. In addition to the above, the least-doped sample shows a very strong resistivity increase at long anneal durations, very similar to the observations in ref. [24] (cf. Figure 5B). The reason
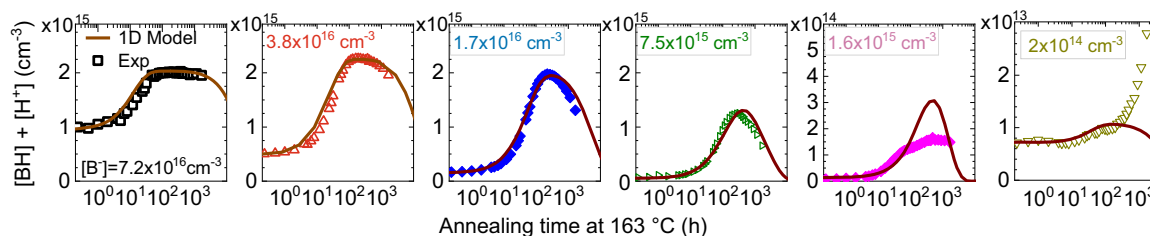

Figure 7. Simulated (brown lines) and measured (symbols, data from [22]) sum of BH and H^+ concentrations in 240 μm-thick FZ wafers with varying doping concentration during dark annealing at 163 °C subsequent to the firing process with 800 °C peak temperature from Figure 6. Note the different y-scales of the two lowly doped samples. The unknown initial BH concentrations in the experimental data are set to the simulated BH concentrations after the firing process to facilitate easy comparison of measurements and simulations.

for this effect is unclear; possibly, the formation of thermal donors is involved.

The fits in ref. [22] were explained by an H^0 dependence of the BH dissolution rate, especially for highly doped samples. In this work, the experimental results of these samples are very well described with a H^+ dominated diffusion. This could be due to 1) the consideration of the depth profile after the firing process or 2) slightly different model parameters. We failed to convincingly reproduce the measurements at high-doped samples with the model presented earlier and an H^0-dominated diffusion and thus explanation (1) is more likely.

4. Conclusion

Hydrogen diffusion processes are crucial for determining the LeTID precursor concentration post-firing and the dynamics of surface degradation. Through successful modeling of BH development during dark annealing (DA) processes across varying temperatures and samples with different doping levels, we have demonstrated that the hydrogen diffusion can explain the observed decrease in BH concentration in the wafer over extended dark annealing periods. Furthermore, the strong alignment of our simulations with measurements following firing processes underscores the necessity of considering the hydrogen depth profiles that result from hydrogen in-diffusion. Due to these diffusion processes, wafer thickness significantly impacts hydrogen dynamics. The comparison with the very comprehensive experimental data shows how well the model and model parameters presented here can be used to predict process steps, and how well industry-related processes can be optimized with regard to hydrogen distribution. Although the model is capable of predicting the dominant hydrogen processes, the behavior observed in low-doped samples (Figure 7 and ref. [22]), and dark annealing experiments conducted above 260 °C (Figure 5 and ref. [24]), indicates the presence of mechanisms not yet accounted for in the model. Additionally, we suggest further experiments to reveal the final location of hydrogen, i.e., in the SiN_x stack or in the surface near-region, and enable calibration of a detailed H model for SiN_x/AlO_x stack systems. While the model is theoretically capable of simulating measurement outcomes under light exposure, discrepancies between experimental results and simulations under illumination at temperatures below 160 °C (see Section I, Supporting Information) indicate that the current model does not account for all H_2 formation mechanisms under illumination.

Supporting Information

Supporting Information is available from the Wiley Online Library or from the author.

Acknowledgements

Conflict of Interest

The authors declare no conflict of interest.

Author Contributions

Jonas Schön: Conceptualization (lead); Data curation (lead); Funding acquisition (supporting); Methodology (lead); Software (lead); Validation (lead); Visualization (lead); Writing—original draft (lead); Writing—review and editing (equal). **Phillip Hamer**: Investigation (supporting); Methodology (supporting); Software (supporting); Writing—original draft (supporting); Writing—review and editing (equal). **Benjamin Hammann**: Conceptualization (supporting); Data curation (equal); Methodology (supporting); Visualization (supporting); Writing—original draft (supporting); Writing—review and editing (supporting). **Christoph Zechner**: Methodology (supporting); Software (supporting); Writing—review and editing (supporting). **Wolfram Kwapil**: Conceptualization (supporting); Funding acquisition (supporting); Supervision (supporting); Writing—original draft (supporting); Writing—review and editing (supporting). **Martin C. Schubert**: Funding acquisition (supporting); Supervision (supporting); Writing—review and editing (supporting).

Data Availability Statement

The data that support the findings of this study are available from the corresponding author upon reasonable request.

Keywords

[1] M. J. Binns, R. C. Newman, S. A. McQuaid, E. C. Lightowlers, *Mater. Sci. Forum* **1993**, *143–147*, 861.

[2] B. J. Hallam, P. G. Hamer, A. M. Ciesla née Wenham, C. E. Chan, B. Vicari Stefani, S. Wenham, *Prog. Photovoltaics Res. Appl.* **2020**, *96*, 173.

[3] P. Hamer, B. Hallam, S. Wenham, M. Abbott, *IEEE J. Photovoltaics* **2014**, *4*, 1252.

[4] C. Herring, N. M. Johnson, C. G. van de Walle, *Phys. Rev. B* **2001**, *64*, 849.

[5] S. J. Pearton, J. W. Corbett, T. S. Shi, *Appl. Phys. A* **1987**, *43*, 153.

[6] M. Stavola, F. Jiang, A. Rohatgi, D. Kim, J. Holt, H. Atwater, J. Kalejs, in *Proc. 3rd WCPEC, Organizing Committee*, Osaka **2003**, pp. 909–912.

[7] M. Stutzmann, W. Beyer, L. Tapfer, C. P. Herrero, *Phys. B: Condens. Matter* **1991**, *170*, 240.

[8] V. V. Voronkov, R. Falster, *Phys. Status Solidi A* **2017**, *214*, 1700287.

[9] D. Chen, M. Vaqueiro Contreras, A. Ciesla, P. Hamer, B. Hallam, M. Abbott, C. Chan, *Prog. Photovoltaics Res. Appl.* **2021**, *29*, 1180.

[10] T. Niewelt, F. Schindler, W. Kwapil, R. Eberle, J. Schön, M. C. Schubert, *Prog. Photovoltaics Res. Appl.* **2017**, *99*, 13701.

[11] J. Schmidt, D. Bredemeier, D. C. Walter, *IEEE J. Photovoltaics* **2019**, *9*, 1497.

[12] R. Eberle, W. Kwapil, F. Schindler, M. C. Schubert, S. W. Glunz, *Phys. Status Solidi RRL* **2016**, *10*, 861.

[13] F. Maischner, S. Maus, J. Greulich, S. Lohmüller, E. Lohmüller, P. Saint-Cast, D. Ourinson, H. Vahlman, K. Hergert, S. Riepe, S. Glunz, S. Rein, *Prog. Photovoltaics Res. Appl.* **2022**, *30*, 123.

[14] M. Winter, D. C. Walter, J. Schmidt, *IEEE J. Photovoltaics* **2023**, *13*, 849.

[15] C. E. Chan, D. N. R. Payne, B. J. Hallam, M. D. Abbott, T. H. Fung, A. M. Wenham, B. S. Tjahjono, S. R. Wenham, *IEEE J. Photovoltaics* **2016**, *6*, 1473.

[16] D. N. R. Payne, C. E. Chan, B. J. Hallam, B. Hoex, M. D. Abbott, S. R. Wenham, D. M. Bagnall, *Phys. Status Solidi RRL* **2016**, *10*, 237.

[17] D. N. Payne, C. E. Chan, B. J. Hallam, B. Hoex, M. D. Abbott, S. R. Wenham, D. M. Bagnall, *Sol. Energy Mater. Sol. Cells* **2016**, *158*, 102.

[18] B. Hammann, N. Assmann, P. M. Weiser, W. Kwapil, T. Niewelt, F. Schindler, R. Sondena, E. V. Monakhov, M. C. Schubert, *IEEE J. Photovoltaics* **2023**, *13*, 224.

[19] V. V. Voronkov, R. Falster, *Phys. Status Solidi B* **2017**, *254*, 1600779.

[20] P. Hamer, B. Hallam, R. S. Bonilla, P. P. Altermatt, P. Wilshaw, S. Wenham, *J. Appl. Phys.* **2018**, *123*, 43108.

[21] D. C. Walter, D. Bredemeier, R. Falster, V. V. Voronkov, J. Schmidt, *Sol. Energy Mater. Sol. Cells* **2019**, *200*, 109970.

[22] P. V. Rodrigues, B. Hammann, N. Aßmann, J. Schön, W. Kwapil, F. Schindler, T. Niewelt, M. C. Schubert, *J. Appl. Phys.* **2024**, *136*, 085703.

[23] Y. Acker, J. Simon, A. Herguth, *Phys. Status Solidi A* **2022**, *219*, 2200142.

[24] C. Winter, J. Simon, A. Herguth, *Phys. Status Solidi A* **2021**, *218*, 2100220.

[25] D. Gomes, V. P. Markevich, A. R. Peaker, J. Coutinho, *Phys. Status Solidi B* **2022**, *259*, 2100670.

[26] P. Hamer, B. Hallam, M. Abbott, C. Chan, N. Nampalli, S. Wenham, *Sol. Energy Mater. Sol. Cells* **2016**, *145*, 440.

[27] A. van Wieringen, N. Warmoltz, *Physica* **1956**, *22*, 849.

[28] R. E. Pritchard, M. J. Ashwin, J. H. Tucker, R. C. Newman, E. C. Lightowlers, M. J. Binns, S. A. McQuaid, R. Falster, *Phys. Rev. B* **1997**, *56*, 13118.

[29] D. Ballutaud, P. de Mierry, J.C. Pesant, R. Rizk, A. Boutry-Forveille, M. Aucouturier, *Mater. Sci. Forum* **1992**, *83–87*, 45.

[30] M. Stutzmann, M. S. Brandt, *J. Appl. Phys.* **1990**, *68*, 1406.

[31] Synopsys, Inc., Sentaurus *Process User Guide*, Mountain View, release U-2022.12, Synopsys, **2022**.

[32] C. Fischer, A. Schmid, A. Herguth, A. Zuschlag, P. P. Altermatt, P. Hamer, G. Hahn, *Sol. Energy Mater. Sol. Cells* **2023**, *250*, 112056.

[33] B. Hammann, N. Aßmann, J. Schön, W. Kwapil, F. Schindler, S. Roder, E. V. Monakhov, M. C. Schubert, *Sol. Energy Mater. Sol. Cells* **2023**, *259*, 112462.

[34] D. Mathiot, *Phys. Rev. B* **1989**, *40*, 5867.

[35] T. Zundel, J. Weber, *Phys. Rev. B* **1989**, *39*, 13549.

[36] V. V. Voronkov, R. Falster, *Mater. Sci. Semicond. Process.* **2023**, *167*, 107796.

[37] W. Kwapil, J. Schön, T. Niewelt, M. C. Schubert, *IEEE J. Photovoltaics* **2020**, *10*, 1591.

[38] D. Bredemeier, D. C. Walter, R. Heller, J. Schmidt, in *36th Eur. Photovoltaic Sol. Energy Conf. Exhib.*, WIP, München **2019**, pp. 112–115.

[39] B. Sopori, Y. Zhang, N. M. Ravindra, *J. Electron. Mater.* **2001**, *30*, 1616.

[40] A. J. Tavendale, A. A. Williams, S. J. Pearton, *MRS Proc.* **1987**, *104*, 285.

[41] J. A. T. de Guzman, V. P. Markevich, J. Coutinho, N.V. Abrosimov, M.P. Halsall, A.R. Peaker, *Solar RRL* **2022**, *6*, 2100459.

[42] Y. Gorelkinskii, N. N. Nevinnyi, *Mater. Sci. Eng. B* **1996**, *36*, 133.

[43] N. M. Johnson, C. Herring, *Phys. Rev. B* **1992**, *46*, 15554.